

The magnetic structures of rare-earth quadruple perovskite manganites RMn_7O_{12}

R. D. Johnson,^{1,*} D. D. Khalyavin,² P. Manuel,² L. Zhang,^{3,4} K. Yamaura,^{3,4} and A. A. Belik³

¹Clarendon Laboratory, Department of Physics, University of Oxford, Oxford, OX1 3PU, United Kingdom

²ISIS facility, Rutherford Appleton Laboratory-STFC, Chilton, Didcot, OX11 0QX, United Kingdom

³Research Center for Functional Materials, National Institute for

Materials Science (NIMS), Namiki 1-1, Tsukuba, Ibaraki 305-0044, Japan

⁴Graduate School of Chemical Sciences and Engineering, Hokkaido University,

North 10 West 8, Kita-ku, Sapporo, Hokkaido 060-0810, Japan

(Dated: March 10, 2024)

We report a neutron powder diffraction study of RMn_7O_{12} quadruple perovskite manganites with $R = \text{La, Ce, Nd, Sm, and Eu}$. We show that in all measured compounds concomitant magnetic ordering of the A and B manganese sublattices occurs on cooling below the Néel temperature. The respective magnetic structures are collinear, with one uncompensated Mn^{3+} moment per formula unit as observed in bulk magnetisation measurements. We show that both $\text{LaMn}_7\text{O}_{12}$ and $\text{NdMn}_7\text{O}_{12}$ undergo a second magnetic phase transition at low temperature, which introduces a canting of the B site sublattice moments that is commensurate in $\text{LaMn}_7\text{O}_{12}$ and incommensurate in $\text{NdMn}_7\text{O}_{12}$. This spin canting is consistent with a magnetic instability originating in the B site orbital order. Furthermore, $\text{NdMn}_7\text{O}_{12}$ displays a third magnetic phase transition at which long range ordering of the Nd sublattice modifies the periodicity of the incommensurate spin canting. Our results demonstrate a rich interplay between transition metal magnetism, orbital order, and the crystal lattice, which may be fine tuned by cation substitution and rare earth magnetism.

I. INTRODUCTION

The quadruple perovskite manganites with chemical formula $AA_3Mn_4O_{12}$ derive from the simple perovskite lattice, and a pattern of large octahedral tilts ($a^+a^+a^+$ in Glazer notation) accommodates a 1:3 ordering of A and A' cations. This chemical order expands the range of manganese-based oxides in which to study the interplay between charge, orbital, and spin degrees of freedom^{1,2}. Furthermore, topological physical properties such as low-field magnetoresistance³ and multiferroic behaviour^{4,5} have been found in the quadruple perovskite manganites.

When $A' = \text{Mn}^{3+}$ a family of manganites is formed that nominally contain Mn^{4+} and Jahn-Teller active Mn^{3+} cations in different proportions on the B sites. The $\text{Mn}^{4+}:\text{Mn}^{3+}$ ratio is determined by the oxidation state of the A cations, which may be monovalent Na^+ , divalent Mn^{2+} , Cd^{2+} , Ca^{2+} , Sr^{2+} , Pb^{2+} , or trivalent R^{3+} ($R = \text{rare earth including Y and Bi}$)⁴⁻¹⁴. Despite the successful synthesis of a large number of quadruple perovskites, the only trivalent A site manganites whose physical properties had been reported prior to our work were $\text{LaMn}_7\text{O}_{12}$,⁸ $\text{PrMn}_7\text{O}_{12}$,⁹ $\text{BiMn}_7\text{O}_{12}$,^{4,15} and $\text{YMn}_7\text{O}_{12}$ ¹⁴.

At high temperature $\text{LaMn}_7\text{O}_{12}$ crystallises in the cubic, $Im\bar{3}$ quadruple perovskite structure¹⁶. As for all $R^{3+}\text{Mn}_7\text{O}_{12}$ compounds every B site is occupied by a Jahn-Teller active Mn^{3+} ion, and below 650 K the crystal symmetry is lowered to monoclinic $I2/m$ as a result of $d_{3z^2-r^2}$ orbital ordering within the ac plane, with nearest neighbour orbitals orientated orthogonal to each other — the same pattern of orbital ordering supported by the simple perovskite LaMnO_3 ^{17,18}. This crystal symmetry and orbital order persists down to low temperature. $\text{BiMn}_7\text{O}_{12}$ and $\text{YMn}_7\text{O}_{12}$ adopt the same pattern

of orbital order as $\text{LaMn}_7\text{O}_{12}$, but the former shows complex structural behaviour as a function of temperature¹⁹, and the latter undergoes a structural phase transition at 200 K that is apparently isostructural¹⁴, yet its origin remains unknown. The structural behaviour of $\text{PrMn}_7\text{O}_{12}$ is complicated by the presence of two polymorphs, one with $I2/m$ symmetry, and the other $R\bar{3}$, which are highly sensitive to synthesis conditions. However, the monoclinic phase fraction is understood to be similar to the La and Bi compounds⁹. $\text{PrMn}_7\text{O}_{12}$ was omitted from the present study due to these structural complications.

$\text{LaMn}_7\text{O}_{12}$ and $\text{BiMn}_7\text{O}_{12}$ are reported to undergo two magnetic phase transitions at $T_1 = 78$ K and $T_2 = 21$ K, and $T_1 = 59$ K and $T_2 = 28$ K, respectively^{4,8}. In $\text{LaMn}_7\text{O}_{12}$ it was found that the B site manganese moments ordered below T_1 with a $\mathbf{k}=(0,0,0)$, antiferromagnetic alignment in the ac plane, with ferromagnetic stacking along the b axis. The A site manganese moments were then found to order independently at T_2 with propagation vector $\mathbf{k}=(0,1,0)$. In $\text{YMn}_7\text{O}_{12}$, the same $\mathbf{k}=(0,0,0)$ antiferromagnetic ordering of B site moments was reported below $T_1 = 108$ K, however, no lower temperature magnetic phase transition was observed. We note that the B site magnetic structure of both compounds is somewhat surprising, as the established orbital order favours ferromagnetic planes stacked antiferromagnetically, as observed in LaMnO_3 ^{20,21}. We discuss this point in detail later.

In this article we report the synthesis and characterisation of polycrystalline samples of RMn_7O_{12} compounds, where $R = \text{La, Ce, Nd, Sm, and Eu}$. We demonstrate that in all measured compounds the A and B manganese sublattices magnetically order concomitantly on cooling below the Néel temperature — contrary to previous reports on $\text{LaMn}_7\text{O}_{12}$ ⁸ and $\text{YMn}_7\text{O}_{12}$ ¹⁴. The refined mag-

netic structure is collinear with one uncompensated A site Mn^{3+} magnetic moment per formula unit, as observed in the bulk magnetisation. We show that both $\text{LaMn}_7\text{O}_{12}$ and $\text{NdMn}_7\text{O}_{12}$ display a second phase transition at low temperature, which is related to a spin canting of the B site sublattice that is commensurate in $\text{LaMn}_7\text{O}_{12}$, and incommensurate in $\text{NdMn}_7\text{O}_{12}$. This spin canting is consistent with an underlying magnetic instability originating in the B site orbital order. Furthermore, $\text{NdMn}_7\text{O}_{12}$ displays a third magnetic phase transition at which long range ordering of the Nd sublattice modifies the periodicity of the incommensurate spin canting. The article is organised as follows. We first present details of the sample synthesis and experimental techniques in Section II. A detailed analysis of neutron powder diffraction data measured from $\text{LaMn}_7\text{O}_{12}$ and $\text{NdMn}_7\text{O}_{12}$ is given in Sections III A and III B, followed by a brief comparison with diffraction data collected on $\text{CeMn}_7\text{O}_{12}$, $\text{SmMn}_7\text{O}_{12}$, and $\text{EuMn}_7\text{O}_{12}$ in Section III C. In Section IV we discuss the results with particular focus on orbital order and bulk magnetisation, and finally, conclusions are drawn in Section V.

II. EXPERIMENT

Polycrystalline $R\text{Mn}_7\text{O}_{12}$ samples with $R = \text{La}, \text{Nd}, \text{Sm},$ and Eu were prepared from stoichiometric mixtures of Mn_2O_3 and $R_2\text{O}_3$ (99.9%). $\text{CeMn}_7\text{O}_{12}$ was prepared from stoichiometric mixtures of Mn_2O_3 , Mn_3O_4 (99.99%), and CeO_2 (99.99%). Single-phase Mn_2O_3 was prepared from commercial MnO_2 (99.99%) by heating in air at 923 K for 24 h. The mixtures were placed in Au or Pt capsules and treated at 6 GPa and about 1570-1670 K for 2 h (heating time to the synthesis temperature was 10 min) in a belt-type high-pressure apparatus. After the heat treatments, the samples were quenched to room temperature, and the pressure was slowly released. All obtained samples were black pellets.

Variable temperature magnetisation measurements of dense pellets from the growth were performed using a SQUID magnetometer (Quantum Design MPMS) on cooling in an applied magnetic field of 1 T from 350 to 2 K. Isothermal magnetization measurements were performed between -7 and 7 T at different temperatures. Neutron powder diffraction measurements were performed on the WISH time-of-flight diffractometer²² at ISIS, the UK Neutron and Muon Spallation Source. Samples were lightly packed into thin 3mm cylindrical vanadium cans to minimise the effects of neutron absorption (large for Sm and Eu), and mounted within a ⁴He cryostat. Data were collected with high counting statistics at a fixed temperature within each magnetic phase, including paramagnetic for reference. Data were also collected with lower counting statistics on warming in the temperature range 1.5 K to 100 K. All diffraction data were refined using Fullprof²³.

III. RESULTS

A. $\text{LaMn}_7\text{O}_{12}$

Variable temperature magnetic susceptibility data measured from our polycrystalline $\text{LaMn}_7\text{O}_{12}$ sample (Figure 3a) showed signatures of two magnetic phase transitions at $T_1 \sim 79.5$ K and $T_2 \sim 22.5$ K, which are both consistent with previous observations⁸. Neutron powder diffraction data collected at 93 K, within the paramagnetic phase of $\text{LaMn}_7\text{O}_{12}$, was fit with a refined model based upon the published crystal structure^{7,8}, and excellent agreement with the data was achieved (Figure 1a). The sample was found to be 95.2 wt% pure, which is typical for samples synthesised under high pressure conditions. Structural parameters are summarised in Table I, where atomic displacement parameters have been omitted as in several compounds strong neutron absorption prevented their reliable determination.

On cooling below T_1 additional magnetic diffraction intensities were observed, which were unambiguously indexed with the propagation vector $\mathbf{k}=(0,0,0)$, as reported⁸. We label this phase AFM I. Symmetry analysis using the ISOTROPY suite^{24,25} showed that two irreducible representations, Γ_1^+ and Γ_2^+ , enter into the decomposition of the magnetic Γ -point reducible representation for the relevant Wyckoff positions (see Table IV of the Appendix for the basis vectors of Γ_1^+ and Γ_2^+). Exhaustive testing of possible magnetic structures found that only one minimal model, which transforms according to Γ_2^+ , faithfully reproduced the neutron diffraction data shown in Figure 1b. The fitted AFM I magnetic structure (Figure 2d) is collinear with all magnetic moments lying within the ac plane. Out of plane tilts of B site moments, which are allowed within the symmetry of Γ_2^+ , did not improve the quality of the fit. The B site moments were ordered antiferromagnetically within the χ mode shown in Figure 2a (for clarity we use χ , α , and γ to denote B site magnetic structure modes typically referred to as C-type, A-type, and G-type, respectively). The A site moments were ordered in a ferrimagnetic structure with two uncompensated moments per unit cell (one moment per formula unit). The refined parameters of the magnetic structure are given in Table II. The moment magnitudes on all A sites were constrained to be the same, as were those on all B sites, and their temperature dependence is shown in Figure 3b.

Our magnetic structure solution for the AFM I phase is different to that previously reported⁸. In particular, we find both A and B sublattices ordering together below T_1 , and both with a $\mathbf{k} = (0,0,0)$ propagation vector. Quantitative evidence for these differences may be found in our neutron diffraction data. The inset of Figure 1b shows the $\{121\}$, $\{\bar{2}11\}$, and $\{\bar{1}12\}$ diffraction intensities in detail, which are mostly magnetic in origin (paramagnetic data is shown in green). The magnetic structure factor of the $\{\bar{2}11\}$ and $\{\bar{1}12\}$ reflections is exactly zero for the collinear B -site order described above, and also

TABLE I. Crystal structure parameters ($I2/m$, $Z = 2$) in the paramagnetic phase of RMn_7O_{12} , with $R = \text{La, Ce, Nd, Sm, and Eu}$ refined at 93, 90, 100, 100, and 100 K, respectively. Wyckoff positions are as follows. A sublattice; R : 2a, Mn1: 2b, Mn2: 2c, Mn3: 2d. B sublattice; Mn4: 4e, Mn5: 4f. Oxygen; O1 & O2: 4i, O3 & O4: 8j. The values of T_1 are given at the bottom.

		LaMn ₇ O ₁₂	CeMn ₇ O ₁₂	NdMn ₇ O ₁₂	SmMn ₇ O ₁₂	EuMn ₇ O ₁₂
Lattice parameters						
a [Å]		7.5219(1)	7.4966(2)	7.4885(1)	7.4854(2)	7.4769(3)
b [Å]		7.36243(8)	7.3511(2)	7.33241(8)	7.3287(2)	7.3246(2)
c [Å]		7.51685(9)	7.4915(2)	7.4850(1)	7.4837(2)	7.4748(2)
β [°]		91.309(1)	91.232(1)	91.256(1)	91.231(2)	91.215(2)
V [Å ³]		416.168(9)	412.75(2)	410.892(9)	410.45(2)	409.27(2)
Fractional coordinates						
O1	x	0.1676(5)	0.1671(5)	0.1666(4)	0.1651(8)	0.1632(8)
	z	0.3084(5)	0.3079(5)	0.3056(4)	0.3055(7)	0.3034(7)
O2	x	0.1783(6)	0.1786(6)	0.1775(6)	0.1781(8)	0.178(1)
	z	0.6882(7)	0.6857(7)	0.6877(6)	0.685(1)	0.687(1)
O3	x	0.0151(4)	0.0153(4)	0.0150(4)	0.0153(6)	0.0146(7)
	y	0.3100(4)	0.3089(4)	0.3084(4)	0.3065(6)	0.3054(6)
	z	0.1722(4)	0.1744(4)	0.1722(4)	0.1737(6)	0.1743(6)
O4	x	0.3125(4)	0.3112(4)	0.3111(3)	0.3107(6)	0.3097(6)
	y	0.1758(4)	0.1755(4)	0.1753(4)	0.1749(6)	0.1739(6)
	z	-0.0137(4)	-0.0123(4)	-0.0126(3)	-0.0123(5)	-0.0124(6)
Fit reliability parameters						
R [%]		3.3	3.65	3.19	3.4	3.3
wR [%]		3.4	4.6	3.28	3.5	3.2
R_{Bragg} [%]		4.6	3.61	3.38	4.9	6.1
Néel temperature						
T_1 [K]		79.5	80	85	87	87

TABLE II. Magnetic structure parameters refined in the AFM I phase of RMn_7O_{12} . Moment directions are given in spherical coordinates defined such that $m_z = m \cos(\theta) \parallel c$, $m_x = m \sin(\theta) \parallel a^*$, and $m_y = 0 \parallel b$. Mn1 and Mn3 moments are parallel, and antiparallel to Mn2 moments. All moments of the Mn4 sublattice are parallel, and antiparallel to those of the Mn5 sublattice.

		LaMn ₇ O ₁₂	CeMn ₇ O ₁₂	NdMn ₇ O ₁₂	SmMn ₇ O ₁₂	EuMn ₇ O ₁₂
T [K]		27	1.5	30	1.5	1.5
Mn1	$m[\mu_B]$	3.51(2)	3.03(3)	3.28(3)	3.45(4)	3.11(6)
	θ [°]	-32.7(3)	-38.7(3)	-33.1(3)	-34.7(4)	-32.1(5)
Mn4	$m[\mu_B]$	2.90(2)	2.97(1)	3.00(2)	3.27(3)	3.24(3)
	θ [°]	-32.7(3)	-38.7(3)	-33.1(3)	-34.7(4)	-32.1(5)
Fit reliability parameters						
R [%]		4.56	4.57	4.19	4.13	6.94
wR [%]		4.58	4.62	4.54	3.59	4.89
R_{Magnetic} [%]		3.85	2.83	4.65	5.81	3.15

zero for the similar B -site order reported in reference 8. Furthermore, it is zero for each Mn4 and Mn5 sublattice, meaning that no degree of in-plane ferromagnetic canting between Mn4 and Mn5 sites, nor different magnitude moments of the two (both giving a net magnetic moment),

can account for the observed intensity at these reflections. Out-of-plane antiferromagnetic canting of B site moments (zero net moment) is allowed by symmetry, as mentioned above. In this case, finite magnetic diffraction intensities would be expected at the $\{\bar{2}11\}$ and $\{\bar{1}12\}$ re-

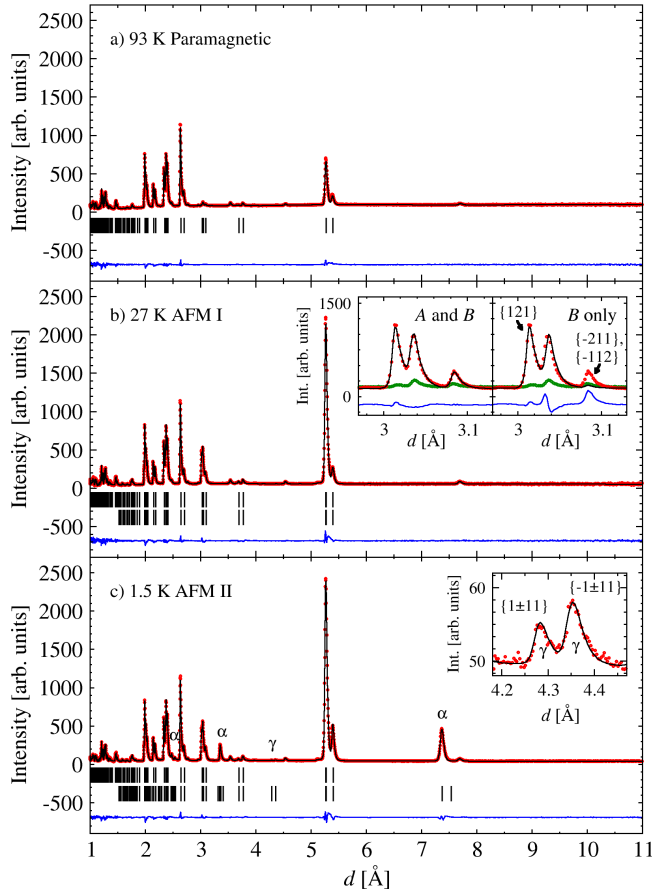


FIG. 1. Neutron powder diffraction data measured from $\text{LaMn}_7\text{O}_{12}$ in bank 2 (average $2\theta = 58.3^\circ$) of the WISH diffractometer. Diffraction data (red points) collected in the paramagnetic, AFM I, and AFM II phases are shown in panes a), b) and c), respectively. The fitted nuclear (top tick marks) and magnetic (bottom tick marks) structural models are shown as a solid black line. Tick marks corresponding to Mn_3O_4 (3.4 wt%), LaMnO_3 (0.5 wt%), and $\text{La}(\text{CO}_3)(\text{OH})$ (0.9 wt%) impurity phases have been omitted for clarity. A difference pattern ($I_{\text{obs}} - I_{\text{calc}}$) is given as a blue solid line at the bottom of each pane.

flections, but at the expense of the $\{121\}$ intensity whose structure factor is exactly zero for this additional b axis component. Indeed, when freely refined, this out-of-plane component was found to be zero within error as it is inconsistent with other magnetic intensities found throughout the diffraction pattern. No other modifications of the collinear B -site structure are consistent with Γ_2^+ symmetry. However, the manganese A site magnetic structure described above does have a non-zero structure factor for the $\{\bar{2}11\}$ and $\{\bar{1}12\}$ reflections, and, combined with the B site order, faithfully reproduces all other diffraction intensities. Hence, given the basic χ -type B site magnetic structure, concomitant $\mathbf{k} = (0,0,0)$ A and B sublattice ordering is unambiguously demonstrated by our neutron diffraction experiments. Furthermore, the A site struc-

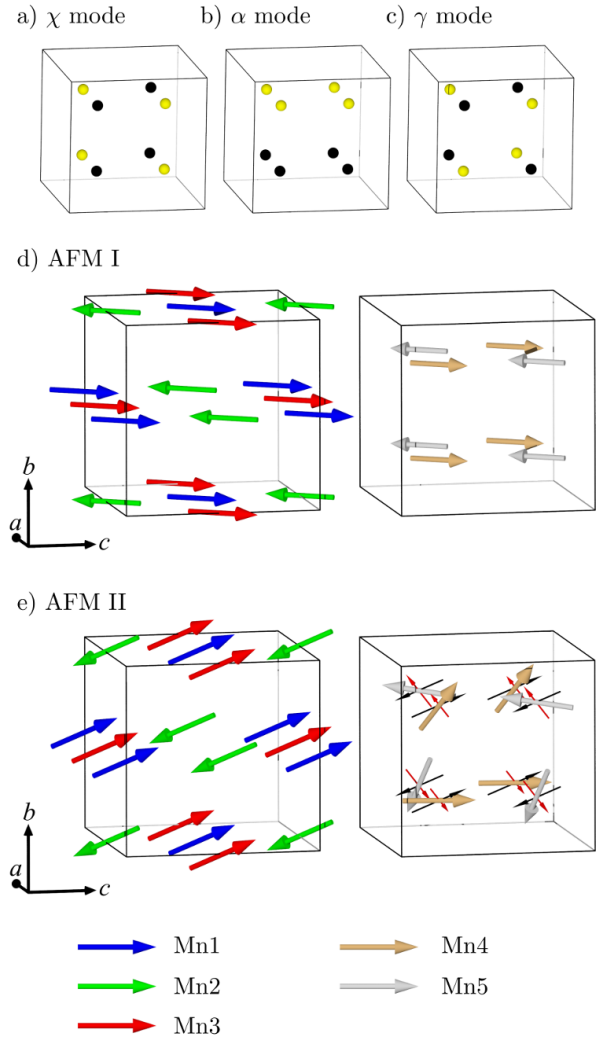


FIG. 2. (a)-(c) Antiferromagnetic modes of the B site sublattice, where yellow and black spheres represent moments of opposite sign. The refined magnetic structures of the AFM I and AFM II phases of $\text{LaMn}_7\text{O}_{12}$ are shown in (d) and (e) respectively, with the A sublattice on the left and the B sublattice on the right. The orthogonal χ and $(\alpha+\gamma)$ components of the ground state B sublattice magnetic structure are shown as thin black and red arrows, respectively. In all panes the $I2/m$ quadruple perovskite unit cell is drawn in black lines.

ture naturally gives rise to an uncompensated $4\mu_B$ per formula unit, as observed in bulk magnetometry measurements (see Figure 9, below).

Below T_2 , three substantial changes in the neutron powder diffraction data occurred simultaneously. Firstly, the relative intensities of the $\mathbf{k} = (0,0,0)$ magnetic diffraction peaks were modified, which could be modelled by a global tilt of the AFM I collinear magnetic structure towards the b axis (Table III). The symmetry of this tilted structure is described by an admixture of Γ_2^+ and Γ_1^+ ir-

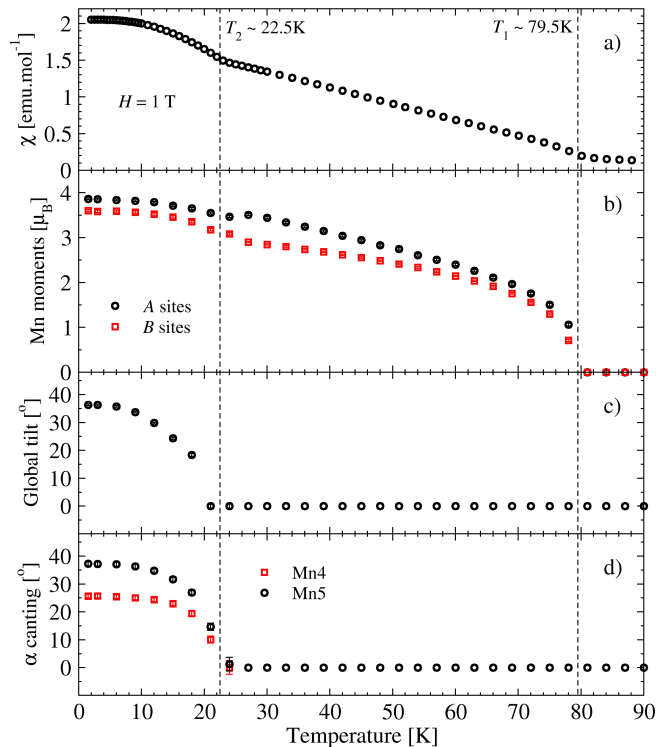


FIG. 3. The $\text{LaMn}_7\text{O}_{12}$ temperature dependence of a) field cooled magnetic susceptibility, b) the A and B site ordered magnetic moments, c) the global tilt of the $\mathbf{k}=(0,0,0)$ magnetic structure component, and d) the canting angle of the Mn4 and Mn5 moments due to the evolution of the $\mathbf{k}=(0,1,0)$ α mode, defined as $\tan^{-1}(m_\alpha/m_\chi)$.

reducible representations, which is allowed below the second magnetic phase transition. The tilt angle is plotted as a function of temperature in Figure 3c, which indeed demonstrates critical behaviour at T_2 . Secondly, an additional family of relatively strong, magnetic diffraction peaks appeared (labelled α in Figure 1c), which could be unambiguously indexed with the propagation vector $\mathbf{k} = (0,1,0)$, as reported⁸. By considering the full set of $\mathbf{k} = (0,1,0)$ reflections, systematic extinctions were observed at, for example, the $\{100\}$, $\{001\}$, $\{120\}$, and $\{021\}$ peak positions. Generic structure factor calculations demonstrated that these extinctions can only arise if the $\mathbf{k} = (0,1,0)$ component of the magnetic structure resides solely on the B sublattice. The same calculations also demonstrated that these new magnetic diffraction peaks are consistent with the α mode illustrated in Figure 2b. Thirdly, two weak reflections were observed as highlighted in the inset of Figure 1c (labelled γ), which also indexed with $\mathbf{k} = (0,1,0)$. These $\{1 \pm 1\}$ and $\{\bar{1} \pm 1\}$ reflections are characteristic of a small γ component of the B sublattice magnetic structure (Figure 2c).

Under the constraint that every magnetic ion should have a saturated magnetic moment in the ground state, the χ and $(\alpha + \gamma)$ components must be orthogonal, giving rise to a noncollinear B sublattice with an average

TABLE III. Magnetic structure parameters refined in the AFM II and AFM II' phases of $\text{LaMn}_7\text{O}_{12}$ and $\text{NdMn}_7\text{O}_{12}$, respectively. Moment directions are given in spherical coordinates defined such that $m_z = m \cos(\theta) \parallel c$, $m_x = m \cos(\phi) \sin(\theta) \parallel a^*$, and $m_y = m \sin(\phi) \sin(\theta) \parallel b$. Parameters given without standard errors have been fixed to maintain a magnetic structure with full moments on all sites. Mn1 and Mn3 moments are parallel, and antiparallel to Mn2 moments. Mn4 and Mn5 moments are given for sites $[\frac{1}{4}, \frac{1}{4}, \frac{1}{4}]$ and $[\frac{1}{4}, \frac{1}{4}, \frac{3}{4}]$, respectively. Moments on the other B sites are transformed by the respective propagation vector.

		$\text{LaMn}_7\text{O}_{12}$	$\text{NdMn}_7\text{O}_{12}$		
T [K]		1.5		1.5	
R	$m[\mu_B]$	-		0.84(3)	
	$\phi[^\circ]$	-		314.6(5)	
	$\theta[^\circ]$	-		150.5(7)	
Mn1	$m[\mu_B]$	3.86(2)		3.73(2)	
	$\phi[^\circ]$	323.7(3)		314.6(5)	
	$\theta[^\circ]$	-45.2(6)		-29.5(7)	
		χ	$\alpha + \gamma$	χ	$\alpha + \gamma$
Mn4	$m[\mu_B]$	3.24(3)	1.56(2)	3.24(3)	0.97(5)
	$\phi[^\circ]$	323.7(3)	-75.8	314.6(5)	-145(2)
	$\theta[^\circ]$	-45.2(6)	52.4(4)	-29.5(7)	96.3
Mn5	$m[\mu_B]$	2.85	2.17(2)	3.02	1.83(5)
	$\phi[^\circ]$	323.7(3)	-75.8	314.6(5)	-145(2)
	$\theta[^\circ]$	134.8(6)	52.4(4)	150.5(7)	96.3
Fit reliability parameters					
R [%]		3.95		5.26	
wR [%]		4.48		5.16	
R_{Magnetic} [%]		2.65		3.87	

spin direction collinear with the A sublattice moments. In this case the small γ component naturally arises if the noncollinearity is different for Mn4 and Mn5 , which is indeed allowed by symmetry. This AFM II magnetic structure is shown in Figure 2e, the refined parameters are given in Table III, and the temperature dependence of the α canting angle is shown in Figure 3, which again displays critical behaviour at T_2 . We note that in order to describe the symmetry of the AFM II magnetic structure it is necessary to mix Y_1^- and Y_2^- (see Table IV of the Appendix), as well as Γ_1^+ and Γ_2^+ irreducible representations. This combination corresponds to a substantial lowering of symmetry to a centrosymmetric triclinic magnetic space group.

B. NdMn₇O₁₂

The field cooled magnetic susceptibility of NdMn₇O₁₂, shown in Figure 6a, demonstrated three magnetic phase transitions at $T_1 = 85$ K, $T_2 = 12$ K, and $T_3 = 8.5$ K. Neutron powder diffraction data collected at 100 K, in the paramagnetic phase of NdMn₇O₁₂, (Figure 4a) was fit with the same $I2/m$ crystal structure model as employed for LaMn₇O₁₂. The model was found to be in excellent agreement with the data, and the refined structural parameters are given in Table I. Furthermore, this analysis demonstrated that our NdMn₇O₁₂ sample was 100% phase pure within the sensitivity of the measurement.

Below T_1 additional magnetic diffraction intensities were observed, which could be indexed with the propagation vector $\mathbf{k}=(0,0,0)$; as was the case for LaMn₇O₁₂. In fact, the diffraction patterns of both compounds below T_1 were found to be qualitatively identical (except for the small impurity peaks present for the La compound). The AFM I magnetic structure model was therefore fit to NdMn₇O₁₂ powder diffraction data measured at 30 K (Figure 4b), and was found to accurately reproduce all magnetic intensities, including the $\{211\}$ and $\{\bar{1}12\}$ reflections that evidence A site magnetic order (Figure 4b inset). The refined AFM I magnetic structure parameters are given in Table II.

In the temperature range $T_3 < T < T_2$, additional magnetic diffraction peaks appeared in positions similar to those observed from LaMn₇O₁₂ below T_2 . However, these peaks could not be indexed with the propagation vector $\mathbf{k}=(0,1,0)$, nor any other commensurate propagation vector corresponding to a high symmetry point of the $I2/m$ Brillouin zone. The highest symmetry incommensurate (ICM) propagation vectors of space group $I2/m$ are either parallel or perpendicular to b^* . Assuming that the ICM propagation vector was close to $(0,1,0)$, the former scenario could be ruled out based upon the absence of $(0,1\pm k_y,0)$ satellites. A systematic search of the reciprocal space plane $(k_x,1,k_z)$ found that the propagation vector $(0.248(2),1,0.064(3))$ reproduced the positions of all magnetic diffraction intensities (> 5 observed). For completeness, the full Brillouin zone was searched and no other solutions were found. On cooling below T_3 there occurred a significant shift in the positions of the ICM diffraction peaks, whilst their intensities continued to increase monotonically. At 1.5 K these peaks could be indexed with the propagation vector $(0.3231(7),1,0.0069(7))$ — further supporting the $(k_x,1,k_z)$ indexing solution. We note that this incommensurate propagation vector is close to the commensurate vector $(1/3,1,0)$, however, the peak positions for $\mathbf{k}=(1/3,1,0)$ are inconsistent with the diffraction data (dashed line in Figure 4d inset). Furthermore, there is no symmetry reason for the propagation vector to lock in at $(1/3,1,0)$ which is neither a high symmetry point in the Brillouin zone nor associated with any pseudo symmetry of the $I2/m$ crystal structure.

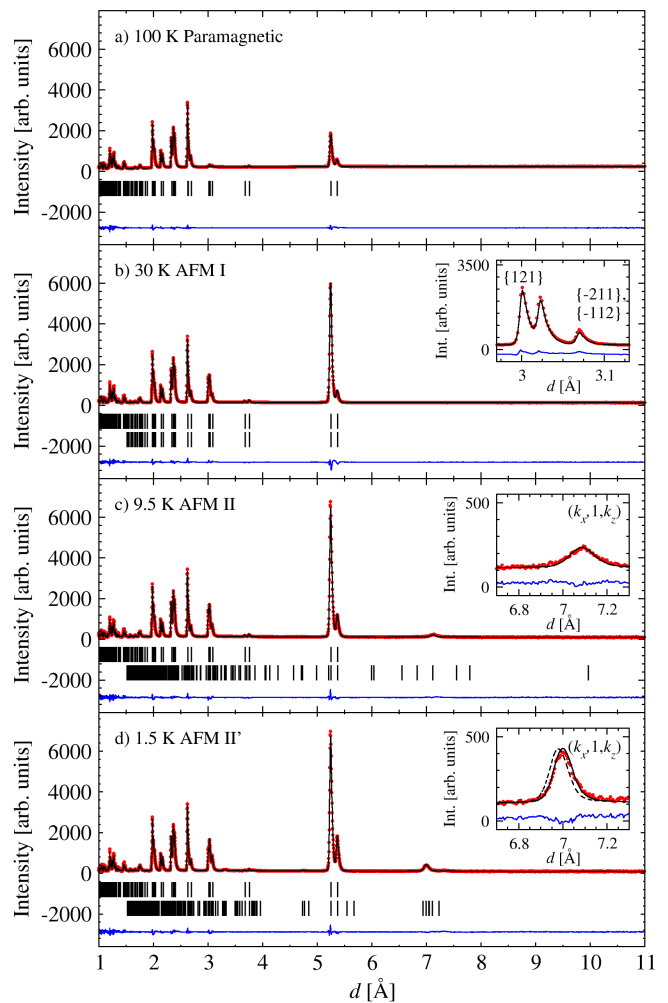


FIG. 4. Neutron powder diffraction data measured from NdMn₇O₁₂ in bank 2 (average $2\theta = 58.3^\circ$) of the WISH diffractometer. Diffraction data (red points) collected in the paramagnetic, AFM I, AFM II, and AFM II' phases are shown in panes a), b), c), and d), respectively. The fitted nuclear (top tick marks) and magnetic (bottom tick marks) structural models are shown as a solid black line. A difference pattern ($I_{\text{obs}} - I_{\text{calc}}$) is given as a blue solid line at the bottom of each pane. The dashed line in the inset to pane d) shows the calculated peak position for the commensurate propagation vector $(1/3,1,0)$.

In both low temperature phases of NdMn₇O₁₂ the additional magnetic diffraction intensities were well fit by the same AFM II model as found for LaMn₇O₁₂, but with the respective ICM propagation vectors assigned to the $(\alpha + \gamma)$ components residing on the B sites (Figures 4c and 4d). To reinforce this similarity we label the $T_3 < T < T_2$ phase of NdMn₇O₁₂ AFM II, and the ground state phase, AFM II'. As before, under the constraint that the magnetic structure has fully saturated moments, the ICM component must be oriented orthogonal to the $\mathbf{k} = (0,0,0)$ component. The B site magnetic structure can then be understood either in terms

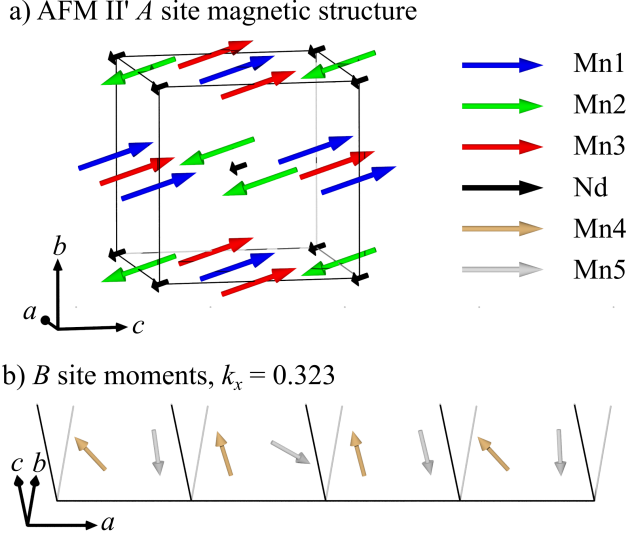


FIG. 5. a) The refined *A* site magnetic structure of the AFM II' phase of $\text{NdMn}_7\text{O}_{12}$. b) The incommensurate 'rocking' of *B* site magnetic moments along the crystallographic *a* axis ($\parallel k_x$). In all panes the $I2/m$ quadruple perovskite unit cell is drawn in faint grey lines.

of a long period planar 'rocking' about the average $\mathbf{k} = (0,0,0)$ direction, or a conical 'rotation' about the average. These two cases are described by an additional spin density wave or cycloidal modulation of the spins, respectively, which, as is typically the case, cannot be readily differentiated by neutron powder diffraction. The ground state magnetic structure of $\text{NdMn}_7\text{O}_{12}$ is illustrated in Figure 5 and parameterised in Table III assuming a rocking type structure. The temperature dependencies of the magnetic structure parameters are shown in Figure 6, including the evolution of the ICM propagation vector.

To maintain a physical value of the Mn^{3+} *A* site magnetic moments below T_3 , *i.e.* $\leq 4\mu_B$, it was necessary to include $\mathbf{k}=(0,0,0)$ magnetic order on the Nd ions, as shown in Figure 6b. Here, ferromagnetically aligned Nd moments of magnitude $0.84(3)\mu_B$ were found to lie antiparallel to the uncompensated moment of the manganese *A* site sublattice. It is well known that in rare earth manganites low temperature magnetic ordering of the rare earth sublattice can modify the magnetic order already present on the manganese sublattice. For example, in NdMnO_3 the Nd ions ferromagnetically order below 15 K with moments of $\sim 1\mu_B$, which drives a spin reorientation of the manganese sublattice and a net magnetisation reversal²⁶. In $\text{NdMn}_7\text{O}_{12}$, the low temperature long range order of the Nd sublattice has two consequences. Firstly, it reduces the macroscopic ferrimagnetic moment, as evidenced in the field cooled magnetic susceptibility of $\text{NdMn}_7\text{O}_{12}$ (Figure 6a). Secondly, Nd ordering can modify the effective exchange coupling between the *A* and *B* sublattices via additional *f-d* exchange interactions. If *A-B* coupling is pivotal

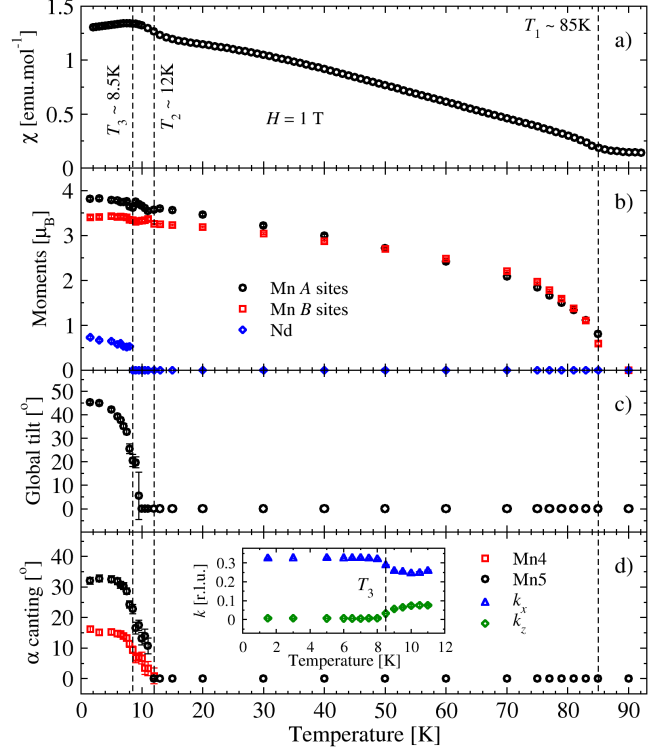


FIG. 6. The $\text{NdMn}_7\text{O}_{12}$ temperature dependence of a) field cooled magnetic susceptibility, b) the *A* site, *B* site, and Nd ordered magnetic moments, c) the global tilt of the $\mathbf{k}=(0,0,0)$ magnetic structure component, and d) the maximum canting angle of the Mn4 and Mn5 moments due to the evolution of the $\mathbf{k}=(k_x, 1, k_z)$ α mode, defined as $\tan^{-1}(m_\alpha/m_\chi)$. The inset of (d) gives the temperature dependence of the incommensurate propagation vector components, k_x and k_z .

in determining the ICM propagation vector, then the long range ordering of the Nd ions can naturally account for the changes in the manganese magnetic structure at T_3 , which do not occur in the case of non-magnetic lanthanum.

C. $\text{CeMn}_7\text{O}_{12}$, $\text{SmMn}_7\text{O}_{12}$, and $\text{EuMn}_7\text{O}_{12}$

Magnetic susceptibility measurements of compounds with $R = \text{Ce}$, Sm , and Eu , shown in Figure 7, demonstrated a single magnetic phase transition; for $\text{CeMn}_7\text{O}_{12}$ $T_1 = 80$ K, and for $\text{SmMn}_7\text{O}_{12}$ and $\text{EuMn}_7\text{O}_{12}$ $T_1 = 87$ K. Neutron powder diffraction data collected in the paramagnetic phase of all three compounds (Figure 8 a-c) was reliably fit with the same $I2/m$ crystal structure model as employed for the $R = \text{La}$ and Nd compounds, and the structural parameters are given in Table I. The $\text{SmMn}_7\text{O}_{12}$ and $\text{EuMn}_7\text{O}_{12}$ samples were found to be 100% phase pure. $\text{CeMn}_7\text{O}_{12}$ was found to be 96% pure, with 3% CeO_2 and 1% Mn_3O_4 impurities present. Furthermore, the $\text{CeMn}_7\text{O}_{12}$ phase was

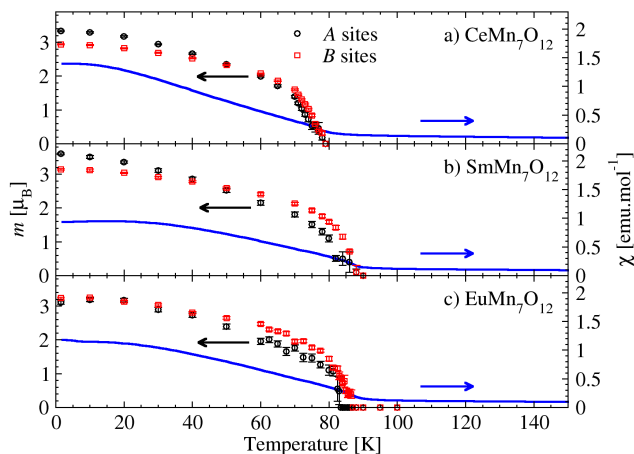


FIG. 7. The temperature dependence of the 1 T field cooled magnetic susceptibility (blue lines) and the AFM I A and B site magnetic moments (black circles and red squares, respectively) of $\text{CeMn}_7\text{O}_{12}$, $\text{SmMn}_7\text{O}_{12}$, and $\text{EuMn}_7\text{O}_{12}$.

found to be non-stoichiometric, with a refined composition of $\text{Ce}_{0.86}\text{Mn}_{7.14}\text{O}_{12}$. In this case Mn^{2+} ions were heterovalently substituted for Ce^{3+} ions, as found for $(\text{Tb}_{0.88}\text{Mn}_{0.12})\text{Mn}_7\text{O}_{12}$ ²⁷, which leads to hole doping on the B sites.

For all three compounds ($R = \text{Ce}, \text{Sm}, \text{and Eu}$), variable temperature neutron powder diffraction experiments confirmed a single magnetic phase from T_1 down to 1.5 K. Magnetic diffraction intensities appeared below T_1 , which could be fit with the $\mathbf{k}=(0,0,0)$ AFM I model (Figure 8 d-f). The respective magnetic structure parameters refined at 1.5 K are given in Table II, and the temperature dependencies of the A and B site moments are shown in Figure 7. For the $\text{SmMn}_7\text{O}_{12}$ and $\text{EuMn}_7\text{O}_{12}$ data analysis an absorption correction was required, based upon a cylindrical geometry as implemented in Fullprof²³

IV. DISCUSSION

As described theoretically by Goodenough, Kanamori, and Anderson^{21,28-30}, orbital order is widely considered to be the primary factor in mediating magnetic exchange in manganese based perovskite oxides and their variants^{20,31-33}. In $\text{RMn}_7\text{O}_{12}$, the orthogonal in-plane ordering of B site Mn^{3+} $d_{3x^2-r^2}$ and $d_{3z^2-r^2}$ orbitals favours ferromagnetic exchange within the ac planes, which are coupled antiferromagnetically along y (α mode), as observed in LaMnO_3 ²⁰. It is surprising, therefore, to find that all measured $\text{RMn}_7\text{O}_{12}$ quadruple perovskites order below T_1 with a B site magnetic structure of antiferromagnetically coupled moments in the ac plane, which are ferromagnetically coupled along b (χ mode) — the exact opposite. Based on the bonding geometry of the perovskite crystal structure one might expect B - B interactions to dominate the magnetic ex-

change energy. However, in $\text{RMn}_7\text{O}_{12}$ the bonding geometry is highly distorted owing to the octahedral tilt pattern that accommodates the ordered occupation of the A site cations. As a result, the B - O - B bonds may be close the critical angle between ferromagnetic and antiferromagnetic exchange, giving rise to the possibility that they are in fact weak with respect to A - A and A - B exchange interactions. The latter interactions would then play the lead role in determining the experimentally observed magnetic structure at the expense of the B - B exchange mediated by orbital order. In $\text{LaMn}_7\text{O}_{12}$ and $\text{NdMn}_7\text{O}_{12}$ an instability towards α type B site magnetic order is apparent below the low temperature phase transitions, which indicates that magnetic frustration due to orbital order plays a key role in the stability of the ground state magnetic structures.

Our neutron powder diffraction results on the evolution of the $\text{RMn}_7\text{O}_{12}$ magnetic structures are further supported by bulk magnetisation measurements. Figure 9 shows the magnetic moment per formula unit of a pressed pellet of our polycrystalline $\text{LaMn}_7\text{O}_{12}$ sample, measured as a function of applied magnetic field. Above T_2 , a remnant moment of approximately $2 \mu_B$ per formula unit was observed in the powder averaged data. Below T_2 , the hysteresis loop narrowed, and the remnant moment increased to $4 \mu_B$ per formula unit — the full uncompensated moment of the A site ferrimagnetic sublattice. This behaviour is consistent with the temperature dependent susceptibility shown in Figure 3a. In pseudocubic symmetry the collinear magnetic structure of the A sublattice is isotropic. In the monoclinic phase this sublattice becomes only weakly anisotropic owing to relatively small distortions away from cubic symmetry. Hence, the magnetic anisotropy of the uncompensated A sublattice moment is likely inherited from coupling to the strongly anisotropic B -sites. This A - B coupling exists only for the $\mathbf{k}=(0,0,0)$ components, by symmetry. The inherited A sublattice anisotropy will therefore be reduced upon α canting of the B sites below T_2 , giving rise to the apparent increase in remnant magnetisation in the powder averaged data of Figure 9. Regarding magnetic anisotropy, one important question remains unanswered: Which anisotropy determines the moment directions in the ground state of $\text{LaMn}_7\text{O}_{12}$ and $\text{NdMn}_7\text{O}_{12}$, giving rise to the global tilt of the magnetic structures?

Finally, it is noteworthy that the low temperature phase transitions to non-collinear ground states have only been observed in compounds with large rare earth ionic radius (La and Nd). However, $\text{CeMn}_7\text{O}_{12}$ appears to be an exception; the ionic radius of Ce is intermediate with respect to La and Nd , yet no low temperature transition was observed. Our $\text{CeMn}_7\text{O}_{12}$ sample was found to be non-stoichiometric, giving rise to hole doping on the Mn B sites. Such doping will diminish the orbital order of the B sites, which is consistent with the suppression of a non-collinear ground state that is otherwise established by magnetic frustration induced by orbital order. To test this observation we measured a non-stoichiometric

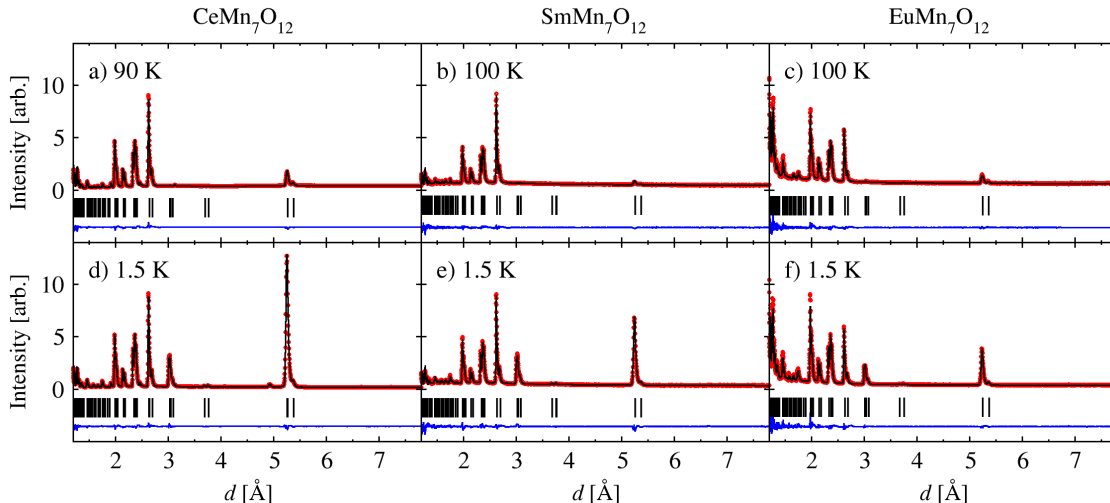


FIG. 8. Neutron powder diffraction data measured from $\text{CeMn}_7\text{O}_{12}$, $\text{SmMn}_7\text{O}_{12}$, and $\text{EuMn}_7\text{O}_{12}$, in bank 2 (average $2\theta = 58.3^\circ$) of the WISH diffractometer. Diffraction data (red points) collected in the paramagnetic and AFM I phases are shown in panes (a-c) and (d-f), respectively. The fitted nuclear and magnetic structural models are shown as solid black lines, with the respective peak positions shown by a single sets of black tick marks. A difference pattern ($I_{\text{obs}} - I_{\text{calc}}$) is given as a blue solid line at the bottom of each pane. Tick marks from impurity phases have been omitted for clarity.

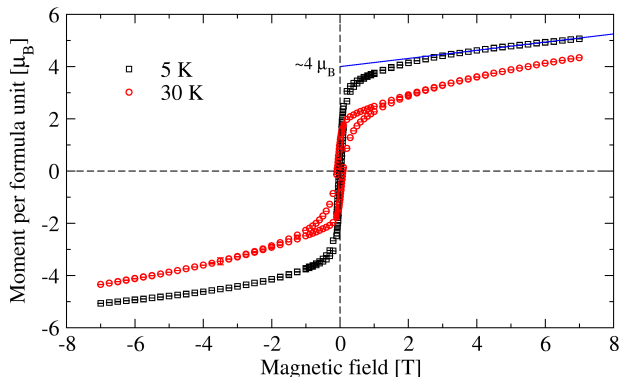


FIG. 9. The magnetic moment per formula unit of our polycrystalline $\text{LaMn}_7\text{O}_{12}$ sample, measured as a function of magnetic field above and below T_2 .

sample of $\text{LaMn}_7\text{O}_{12}$ (composition $\text{La}_{0.9}\text{Mn}_{7.1}\text{O}_{12}$), in which we observed weak anomalies in the heat capacity and magnetic susceptibility at T_2 , and broad $\mathbf{k}=(0,1,0)$ magnetic diffraction peaks below T_2 (not shown here). Both observations are evidence of the suppression of the non-collinear ground state. Furthermore, variable temperature neutron powder diffraction data measured from $\text{La}_{0.9}\text{Mn}_{7.1}\text{O}_{12}$, also not shown here, demonstrated a reduction of T_1 by 3.5 K, which was also observed upon increasing x in $(\text{Tb}_{1-x}\text{Mn}_x)\text{Mn}_7\text{O}_{12}$ ²⁷.

V. CONCLUSIONS

In all measured $\text{RMn}_7\text{O}_{12}$ compounds we have found that the A and B manganese sublattices magnetically order concomitantly on cooling below the first magnetic phase transition at T_1 (between 80 and 90 K). The magnetic structure (labelled AFM I throughout) is collinear, with one uncompensated A site Mn^{3+} magnetic moment per formula unit. This uncompensated moment naturally explains the bulk magnetisation measured throughout the magnetic phases. In $\text{LaMn}_7\text{O}_{12}$ and $\text{NdMn}_7\text{O}_{12}$ a second phase transition occurs at low temperature (T_2), which we have shown to be related to the onset of a secondary component of the magnetic structure associated with the B site sublattice. In $\text{LaMn}_7\text{O}_{12}$ this component is commensurate, and in $\text{NdMn}_7\text{O}_{12}$ it is incommensurate, but in both cases it likely reflects a magnetic instability originating in the B site orbital order. In this regard the $\text{RMn}_7\text{O}_{12}$ compounds appear to be somewhat unconventional, as the magnetic order is not primarily determined by the underlying orbital order, as would be expected in the manganites. Our results might be explored further in both theoretical and experimental studies of the magnetic exchange interactions of $\text{RMn}_7\text{O}_{12}$, and the microscopic distinctions between these materials and, for example, the $\text{A}^{1+,2+}\text{Mn}_7\text{O}_{12}$ quadruple perovskites and the RMnO_3 simple perovskites.

ACKNOWLEDGMENTS

RDJ acknowledges support from a Royal Society University Research Fellowship, and fruitful discussions with

Dr. F. Orlandi. The work performed in Japan was

supported in part by JSPS KAKENHI, Grant Numbers JP15K14133 and JP16H04501.

-
- * roger.johnson@physics.ox.ac.uk
- ¹ A. N. Vasilev and O. S. Volkova, *Low Temperature Physics* **33**, 895 (2007).
 - ² E. Gilioli and L. Ehm, *IUCrJ* **1**, 590 (2014).
 - ³ Z. Zeng, M. Greenblatt, M. A. Subramanian, and M. Croft, *Phys. Rev. Lett.* **82**, 3164 (1999).
 - ⁴ F. Mezzadri, G. Calestani, M. Calicchio, E. Gilioli, F. Bolzoni, R. Cabassi, M. Marezio, and A. Migliori, *Phys. Rev. B* **79**, 100106 (2009).
 - ⁵ R. D. Johnson, L. C. Chapon, D. D. Khalyavin, P. Manuel, P. G. Radaelli, and C. Martin, *Phys. Rev. Lett.* **108**, 067201 (2012).
 - ⁶ M. Marezio, P. Dernier, J. Chenavas, and J. Joubert, *Journal of Solid State Chemistry* **6**, 16 (1973).
 - ⁷ B. Bochu, J. Chenavas, J. Joubert, and M. Marezio, *Journal of Solid State Chemistry* **11**, 88 (1974).
 - ⁸ A. Prodi, E. Gilioli, R. Cabassi, F. Bolzoni, F. Licci, Q. Huang, J. W. Lynn, M. Affronte, A. Gauzzi, and M. Marezio, *Phys. Rev. B* **79**, 085105 (2009).
 - ⁹ F. Mezzadri, M. Calicchio, E. Gilioli, R. Cabassi, F. Bolzoni, G. Calestani, and F. Bissoli, *Phys. Rev. B* **79**, 014420 (2009).
 - ¹⁰ T. Locherer, R. Dinnebier, R. Kremer, M. Greenblatt, and M. Jansen, *Journal of Solid State Chemistry* **190**, 277 (2012).
 - ¹¹ S. V. Ovsyannikov, A. M. Abakumov, A. A. Tsirlin, W. Schnelle, R. Egoavil, J. Verbeeck, G. VanTendeloo, K. V. Glazyrin, M. Hanfland, and L. Dubrovinsky, *Angewandte Chemie International Edition* **52**, 1494 (2013).
 - ¹² Y. S. Glazkova, N. Terada, Y. Matsushita, Y. Katsuya, M. Tanaka, A. V. Sobolev, I. A. Presniakov, and A. A. Belik, *Inorganic Chemistry* **54**, 9081 (2015).
 - ¹³ A. A. Belik, Y. S. Glazkova, N. Terada, Y. Matsushita, A. V. Sobolev, I. A. Presniakov, N. Tsujii, S. Nimori, K. Takehana, and Y. Imanaka, *Inorganic Chemistry* **55**, 6169 (2016).
 - ¹⁴ M. Verseils, F. Mezzadri, D. Delmonte, B. Baptiste, Y. Klein, S. Shcheka, L. C. Chapon, T. Hansen, E. Gilioli, and A. Gauzzi, *Phys. Rev. Materials* **1**, 064407 (2017).
 - ¹⁵ N. Imamura, M. Karppinen, T. Motohashi, D. Fu, M. Itoh, and H. Yamauchi, *J. Am. Chem. Soc.* **130**, 14948 (2008).
 - ¹⁶ H. Okamoto, M. Karppinen, H. Yamauchi, and H. Fjellvg, *Solid State Sciences* **11**, 1211 (2009).
 - ¹⁷ Y. Murakami, J. P. Hill, D. Gibbs, M. Blume, I. Koyama, M. Tanaka, H. Kawata, T. Arima, Y. Tokura, K. Hirota, and Y. Endoh, *Phys. Rev. Lett.* **81**, 582 (1998).
 - ¹⁸ G. Matsumoto, *Journal of the Physical Society of Japan* **29**, 606 (1970).
 - ¹⁹ A. A. Belik, Y. Matsushita, Y. Kumagai, Y. Katsuya, M. Tanaka, S. Y. Stefanovich, B. I. Lazoryak, F. Oba, and K. Yamaura, *Inorganic Chemistry* **56**, 12272 (2017).
 - ²⁰ E. O. Wollan and W. C. Koehler, *Physical Review* **100**, 545 (1955).
 - ²¹ J. B. Goodenough, *Phys. Rev.* **100**, 564 (1955).
 - ²² L. C. Chapon, P. Manuel, P. G. Radaelli, C. Benson, L. Perrott, S. Ansell, N. J. Rhodes, D. Raspino, D. Duxbury, E. Spill, and J. Norris, *Neutron News* **22**, 22 (2011).
 - ²³ J. Rodríguez-Carvajal, *Physica B* **192**, 55 (1993).
 - ²⁴ B. J. Campbell, H. T. Stokes, D. E. Tanner, and D. M. Hatch, *J. Appl. Crystallogr.* **39**, 607 (2006).
 - ²⁵ H. T. Stokes, D. M. Hatch, and B. J. Campbell, "Isotropy," (2007).
 - ²⁶ A. Kumar, S. M. Yusuf, and C. Ritter, *Phys. Rev. B* **96**, 014427 (2017).
 - ²⁷ L. Zhang, N. Terada, R. D. Johnson, D. D. Khalyavin, P. Manuel, Y. Katsuya, M. Tanaka, Y. Matsushita, K. Yamaura, and A. A. Belik, *Inorganic Chemistry* **57**, 5987 (2018), pMID: 29722530.
 - ²⁸ P. W. Anderson, *Phys. Rev.* **79**, 350 (1950).
 - ²⁹ J. Kanamori, *J. Theoret. Phys.* **17**, 197 (1957).
 - ³⁰ J. B. Goodenough, *Journal of Physics and Chemistry of Solids* **6**, 287 (1958).
 - ³¹ P. G. Radaelli, D. E. Cox, M. Marezio, and S. W. Cheong, *Physical Review B* **55**, 3015 (1997).
 - ³² Y. Tokura, *Reports on Progress in Physics* **69**, 797 (2006).
 - ³³ R. D. Johnson, D. D. Khalyavin, P. Manuel, P. G. Radaelli, I. S. Glazkova, N. Terada, and A. A. Belik, *Phys. Rev. B* **96**, 054448 (2017).

Appendix A: Irreducible representations for the commensurate propagation vectors

TABLE IV. Basis vectors of the irreducible representations used to describe the commensurate magnetic structures of $R\text{Mn}_7\text{O}_{12}$. Sites related by I centring (not listed here) respect the propagation vector according to the phase $2\pi\mathbf{k} \cdot \mathbf{r}$. A cartesian basis is adopted, where $x||a^*$, $y||b$, and $z||c$.

\mathbf{k}	Γ_1^+	Γ_2^+	Y_1^-	Y_2^-
	(0,0,0)	(0,0,0)	(0,1,0)	(0,1,0)
Mn1, $0, \frac{1}{2}, 0$	[0,1,0]	[1,0,0] [0,0,1]	- -	- -
Mn2, $\frac{1}{2}, 0, 0$	[0,1,0]	[1,0,0] [0,0,1]	- -	- -
Mn3, $\frac{1}{2}, \frac{1}{2}, 0$	[0,1,0]	[1,0,0] [0,0,1]	- -	- -
Mn4, $\frac{1}{4}, \frac{1}{4}, \frac{1}{4}$	[1,0,0] [0,1,0] [0,0,1]	[1,0,0] [0,1,0] [0,0,1]	[1,0,0] [0,1,0] [0,0,1]	[1,0,0] [0,1,0] [0,0,1]
Mn4, $\frac{1}{4}, \frac{3}{4}, \frac{1}{4}$	$[\bar{1}, 0, 0]$ [0,1,0] [0,0, $\bar{1}$]	[1,0,0] [0, $\bar{1}$,0] [0,0,1]	[1,0,0] [0, $\bar{1}$,0] [0,0,1]	$[\bar{1}, 0, 0]$ [0,1,0] [0,0, $\bar{1}$]
Mn5, $\frac{3}{4}, \frac{1}{4}, \frac{1}{4}$	[1,0,0] [0,1,0] [0,0,1]	[1,0,0] [0,1,0] [0,0,1]	[1,0,0] [0,1,0] [0,0,1]	[1,0,0] [0,1,0] [0,0,1]
Mn5, $\frac{3}{4}, \frac{3}{4}, \frac{1}{4}$	$[\bar{1}, 0, 0]$ [0,1,0] [0,0, $\bar{1}$]	[1,0,0] [0, $\bar{1}$,0] [0,0,1]	[1,0,0] [0, $\bar{1}$,0] [0,0,1]	$[\bar{1}, 0, 0]$ [0,1,0] [0,0, $\bar{1}$]